

Bismuth antiphase domain wall: A three-dimensional manifestation of the Su-Schrieffer-Heeger model

Jinwoong Kim¹, Cheng-Yi Huang^{1,2}, Hsin Lin³, David Vanderbilt⁴, and Nicholas Kioussis¹
¹ Department of Physics and Astronomy, California State University, Northridge, California 91330, USA
² Department of Physics, Northeastern University, Boston, Massachusetts 02115, USA
³ Institute of Physics, Academia Sinica, Taipei 11529, Taiwan and
⁴ Department of Physics and Astronomy, Rutgers University, Piscataway, New Jersey 08854-8019, USA
(Dated: January 12, 2023)

The Su, Schrieffer and Heeger (SSH) model, describing the soliton excitations in polyacetylene due to the formation of antiphase domain walls (DW) from the alternating bond pattern, has served as a paradigmatic example of one-dimensional (1D) chiral topological insulators. While the SSH model has been realized in photonic and plasmonic systems, there have been limited analogues in three-dimensional (3D) electronic systems, especially regarding the formation of antiphase DWs. Here, we propose that pristine bulk Bi, in which the dimerization of (111) atomic layers renders alternating covalent and van der Waals bonding within and between successive (111) bilayers, respectively, serves as a 3D analogue of the SSH model. First, we confirm that the two dimerized Bi structures belong to different Zak phases of 0 and π by considering the parity eigenvalues and Wannier charge centers, while the previously reported bulk topological phases of Bi remain invariant under the dimerization reversal. Next, we demonstrate the existence of topologically non-trivial (111) and trivial (11 $\bar{2}$) DWs in which the number of in-gap DW states (ignoring spin) is odd and even respectively, and show how this controls the interlinking of the Zak phases of the two adjacent domains. Finally, we derive general criteria specifying when a DW of arbitrary orientation exhibits a π Zak phase based on the flip of parity eigenvalues. An experimental realization of dimerization in Bi and the formation of DWs may be achieved via intense femtosecond laser excitations that can alter the interatomic forces and bond lengths.

I. INTRODUCTION

Polyacetylene,¹ $(\text{CH})_x$, is an infinite one-dimensional (1D) carbon chain whose *trans* configuration has two degenerate dimerized structures consisting of alternating double and single bonds which can be interchanged by symmetry. Interestingly, polyacetylene exhibits finite electric conductivity even though its intrinsic band structure is insulating. This can be understood in terms of the migration of electrically-charged antiphase domain walls (DWs) between two structures (domains) with opposite dimerization as illustrated in Fig. 1 (a-c). The Su-Schrieffer-Heeger (SSH) model,^{2,3} introduced to describe polyacetylene, yields a transition from a trivial to topological non-trivial phase depending on the relative hopping amplitudes between the two distinct types of bondings, where the so-called “winding number” undergoes a discontinuous change from $0 \rightarrow 1$. The “winding number” is closely related to the Zak phase⁴ which is quantized to be 0 or π for systems with space inversion symmetry. Moreover, the DW in the SSH model leads to the emergence of a boundary localized zero-energy mode in the middle of the energy gap with charge accumulation of $\pm e/2$, analogous to the fractionally charged excitations in quantum field theory. This midgap state is understood as a topologically protected boundary mode and the SSH model serves as a paradigmatic example of topological insulator protected by a chiral (i.e., sublattice) symmetry.

The SSH model is the simplest and one of the most important models in describing band topology in condensed matter physics, and has been the subject of in-

tense investigations such as Majorana zero mode in a finite atomic chain^{5,6} and an extension to two-dimensional (2D) systems, including graphene⁷ and four-basis-^{8,9} and two-basis-¹⁰ square-lattice models. The latter study¹⁰ explicitly characterized several topological phases with distinct winding numbers upon uniaxial strain and sublattice dimerization where zero-energy flat bands were predicted to emerge on 1D antiphase DW if the winding numbers (equivalently the Zak phases) of the two facing domains are different. This is the 2D analogue of the SSH model.

In three-dimensional (3D) systems, non-trivial π Zak phases have drawn less attention and only a few systems have been found to exhibit them.^{11,12} Sc_2C , a designed inorganic electride,¹³ was predicted to exhibit a π Zak phase with consequent surface states inside its insulating band gap.¹¹ Surface drum-head states of topological nodal-line semimetals are also known to originate from the π Zak phase,^{14–16} where the drum-head states are bounded by surface-projected bulk nodal lines, in contrast to the π Zak phase insulator. For example, Sc_2C (Y_2C) is a π Zak phase insulator (topological nodal-line semimetal) where the surface states cover 100% (90.4%) of the surface BZ.¹¹ The {111} surfaces of silicon and diamond host surface bands from the π Zak phase,¹² where each surface unit cell accumulates one half of an electron¹⁷ leading to half-filled metallic surface bands. An insulating surface can be achieved only by even-number (such as 2×2) surface reconstructions that allow an integer number of surface electrons and hence fully filled bands.^{12,18} The 3D π Zak phase systems that have been reported so far involve no atomic displacement that

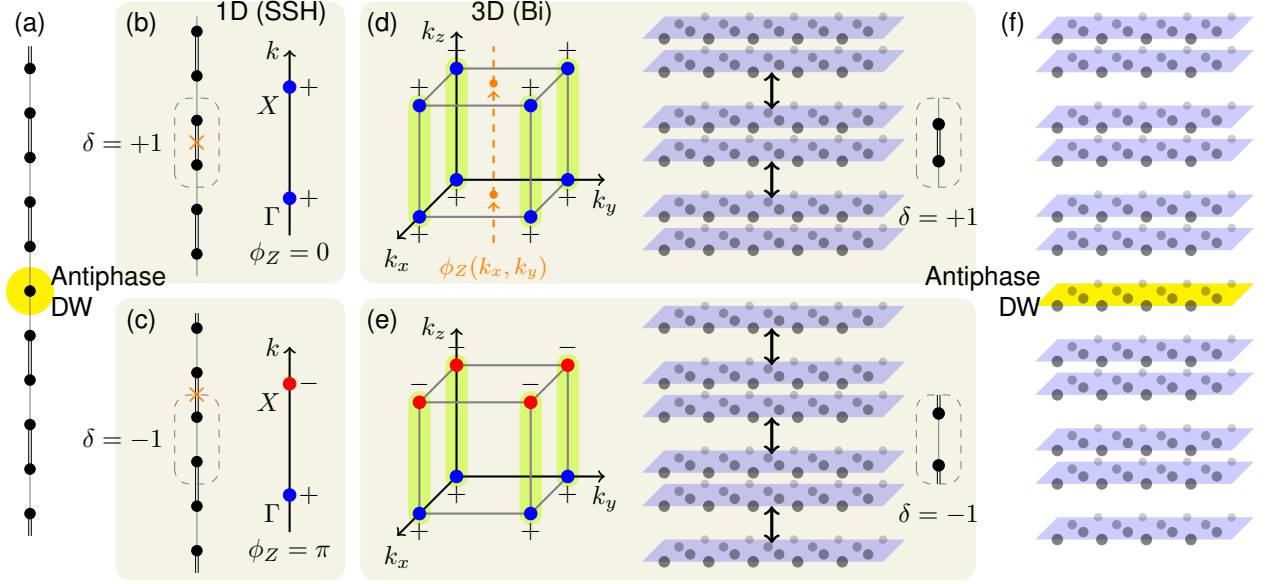


FIG. 1. Schematic view of the SSH model and comparison with the 3D analogue. (a) Antiphase DW of the SSH model where two atomic chains with alternating weak and strong bonding are connected out of phase. (b) and (c) Two dimerized phases ($\delta = \pm 1$) and corresponding parity eigenvalues at the two time-reversal invariant momenta (TRIM), Γ and X , whose product determines the Zak phase ($\phi_Z = 0, \pi$). Dashed box denotes the repeating unit cell where weak (strong) bonds are trimmed at the cell boundary for $\delta = +1$ ($\delta = -1$). Red crosses indicate the (net) Wannier charge center \bar{r} . (d) and (e) Parity eigenvalues at the eight TRIM points of the 3D SSH model for the two dimerized $\delta = \pm 1$ phases shown on the right, with strong (weak) intra- (inter-) bilayer bonding. The shaded vertical lines in momentum space correspond to four individual 1D SSH models in the presence of inversion and time-reversal symmetries whose Zak phase is quantized and flipped by the dimerization reversal in analogy to the SSH model. Vertical dashed line in (d) illustrates the closed 1D path, $k_z \in [0, 2\pi]$ along which the Zak phase is defined. (f) Antiphase DW as the 3D analogue of the SSH model where the Zak-phase-induced in-gap states emerge at the four interface TRIM points, spatially localized at the central (yellow) layer.

can be described as a dimerization. In this work, we show that each (111) atomic layer of Bi corresponds to a single site of the 1D SSH model, and dimerization of the atomic layers in the ground state results in 0 or π Zak phases depending on the dimerization sign, $\delta = \pm 1$, as illustrated in Fig. 1(d-e).

The Zak phase⁴ is a special form of the Berry phase¹⁹ and is equivalent to the electronic part of the polarization,^{17,20,21}

$$\phi_Z = \phi_B = \frac{2\pi p}{ec}, \quad (1)$$

where $-e$ is the electron charge, c is the lattice constant of the unit cell, and p is the dipole moment of the bulk unit cell that can be in turn expressed in terms of the Wannier functions of the occupied bands,

$$p = - \sum_i^{\text{occ.}} e r_i. \quad (2)$$

Here, r_i is the center of i -th Wannier function. In the presence of inversion symmetry, the dipole moment is quantized such that the Zak phase can only take on values $\phi_Z = 0$ or π , corresponding to whether the net Wannier center $\bar{r} = \sum_i r_i$ is located at the center ($\bar{r} = 0$) or the boundary ($\bar{r} = c/2$) of the bulk unit cell, respectively

(see Fig. 1(b,c)). This definition depends on the choice of inversion center for the placement of the origin, which we assume to have been decided once and for all. The origin-dependent Zak phase has been discussed in detail by introducing the ‘‘intercellular Zak phase’’.²² The Zak phase can be easily computed from the product of the parity eigenvalues of the occupied bands at time-reversal invariant momenta (TRIM)^{23,24} in the 1D momentum space, where $\phi_Z = 0$ (π) corresponds to positive (negative) product as shown in Fig. 1 (b) (Fig. 1 (c)).

In 2D and 3D systems, the Zak phase can be defined on a closed 1D path such as a periodic k_z string with a fixed in-plane momentum (k_x, k_y) as shown in Fig. 1(d). Under inversion and time-reversal symmetry and in the absence of SOC, an insulating bulk has a constant and quantized Zak phase on such strings normal to a given surface regardless of the specific in-plane momentum (k_x, k_y) . This implies that a single pair of surface-projected TRIM is enough to determine the Zak phase of the entire surface, $\phi_Z(k_x, k_y) = \phi_Z(0, 0) = \{0, \pi\}$. Turning on the SOC, however, allows modulation of the Zak phase which is no longer quantized at generic surface momenta except at the surface TRIM. Because of the strong SOC of Bi, we focus on the four surface TRIM where the Zak phase is quantized to be 0 or π (see shaded lines in Fig. 1(d,e) connecting the four pairs of TRIM).

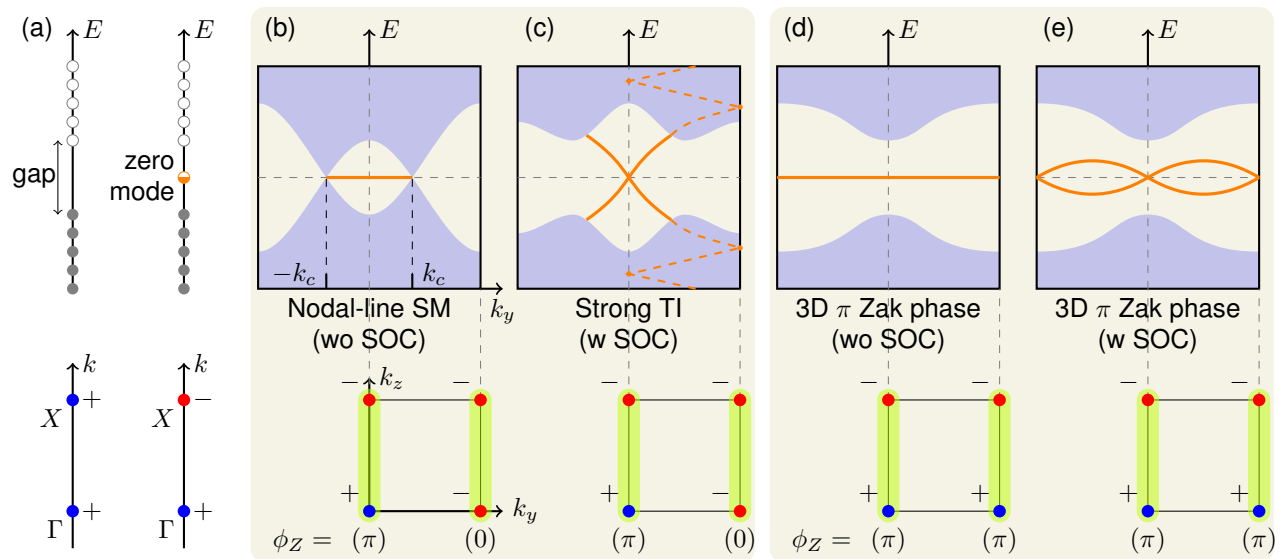


FIG. 2. Schematic view of the Zak phase, $\phi_Z(k_x = 0, k_y)$ and relevant boundary states in several topological systems. Lower (upper) panels illustrate the parity eigenvalues at TRIM points (boundary band structure). (a) 1D SSH model. Open (closed) circles denote empty (filled) states of the zero-dimensional boundary. Non-trivial π Zak phase on the right side induces a half-filled zero mode at the Fermi level. (b-e) $k_x = 0$ plane of the 3D momentum space and its surface (normal to z) band structure without and with SOC. Orange solid lines (shaded areas) denote surface (surface-projected bulk) states. (b) Nodal-line semimetal whose quantized Zak phase is π and 0 for $|k_y| < |k_c|$ and $|k_y| > |k_c|$, respectively. The continuous zero mode at $|k_y| < |k_c|$ forms drum-head states, connecting boundary-projected bulk nodal lines. (c) Strong topological insulator with a surface Dirac cone which emerges at a surface TRIM with π Zak phase. Dashed orange lines illustrate surface band connectivity between surface TRIM, referred to as “switch partners”. (d) and (e) 3D π Zak phase without and with SOC, respectively. In the presence of SOC, the Zak phase is no longer quantized except at the surface TRIM and the in-gap state splits at generic momentum k .

Figure 2 illustrates schematically the boundary states of various topological phases and the corresponding Zak phase configurations at the surface TRIM points. Hirayama *et al.*¹¹ demonstrated that the surface states of the 3D π Zak phase (Fig. 2(d)) is a full-BZ extension of the drum-head states of a nodal-line semimetal (Fig. 2(b)). This can be understood as a continuous shift of $k_c \rightarrow \pi$ that accompanies a band inversion at $k_y = \pi$ and switching of the Zak phase $\phi_Z(0, \pi)$ from 0 to π . In the presence of SOC, the degeneracy of the bulk nodal lines is lifted and the system becomes a strong topological insulator (STI) as shown in Fig. 2(c). Note that the Zak phases $\phi_Z(0, 0) = \pi$ and $\phi_Z(0, \pi) = 0$ do not change. In contrast to the STI phase where a robust surface state is guaranteed by the “switch partners” band connectivity between TRIM,^{23,24} the surface state induced by the π Zak phase is rather isolated in energy from the valence and conduction bands (Fig. 2(e)). The surface band can be pushed into the valence or conduction bands via surface modifications unless it is protected by a chiral (or particle-hole) symmetry which in turn pins the non-trivial surface state at the Fermi level. Since the Bi p bands are well separated from the lower energy s bands and the inter-sublattice hopping matrix elements ($\sigma_{w,v}$ in Appendix A) are dominant there is an effective chiral symmetry which retains the non-trivial state within the

bandgap of the Bi antiphase DW.

In this work we propose that the α -phase of bulk Bi in the rhombohedral structure is a 3D analogue of the 1D SSH system. In Sec. II using DFT-parameterized tight-binding model calculations we investigate the topological properties of the two dimerized states of bulk Bi. We find that the dimerization reversal induces parity sign flip at four TRIM (without changing the bulk topology) which in turn induce a transition of the Zak phase from $\pi \rightarrow 0$, consistent with the emergence of odd or even number of Wannier charge centers (WCCs) at the cell boundary. In Sec. III A we consider two types of (111) DWs sandwiched between two oppositely dimerized states and show the emergence of topologically-protected DW localized states, in contrast to the trivial DW states for the (11 $\bar{2}$) DWs discussed in Sec. III B. In Sec. III C we derive criteria for the emergence of π and 0 Zak phases for a DW of arbitrary orientation and identify those DW orientations that host non-trivial DW states. Sec. III D discusses a plausible experimental realization of the dimerization reversal in pristine Bi and the formation of DW using intense femtosecond laser excitations that can alter the interatomic forces and energy barriers between the two dimerized states.²⁵ Conclusions are summarized in Sec. IV and Sec. V describes the methodology used. Our findings suggest a novel band engineering concept

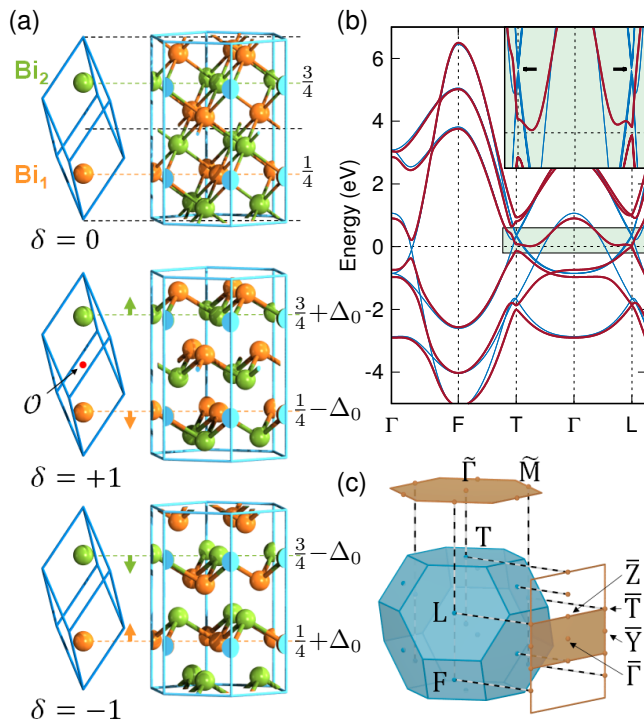


FIG. 3. (a) The primitive cell of Bi with two sublattice sites at fractional height $1/2 \pm (1/4 + \Delta)$ along the $[111]$ direction, where Δ is the Bi displacement $\delta = \Delta/\Delta_0 = \pm 1$ is the dimerization sign, and Δ_0 is the equilibrium displacement. Top panel denotes the unstable undimerized state ($\delta = 0$) and the two lower panels denote the stable dimerized states ($\delta = \pm 1$). Dimerized Bi atomic layers, stacked along $[111]$, are illustrated in the conventional hexagonal cell on the right. The inversion center \mathcal{O} located at the center of the primitive cell is marked with the red dot. (b) The calculated bulk band structure using tight-binding parameters obtained from first-principles calculations (see Appendix A). Red (blue) lines denote the stable dimerized (unstable undimerized) structure. Inset: Zoom-in band structure near the T and L points showing the narrow gap and gap-closing (marked by arrows) for the dimerized and undimerized structures, respectively. (c) First Brillouin zone (BZ) of bulk Bi and its projection on the (111) and $(11\bar{2})$ interface BZs.

for topologically protected states using antiphase DWs where the parity sign flip can occur without the assistance of strong spin-orbit coupling of heavy ions.

II. BULK BI: DIMERIZATION AND TOPOLOGY

Atomic structure – The α -phase of bulk Bi in the rhombohedral structure (space group $R\bar{3}m$, No. 166) is shown in Fig. 3(a), where the conventional unit cell has a bilayer (BL) structure with an ABC stacking sequence along the $[111]$ direction consisting of three BLs. There is strong covalent bond within each BL (intra-BL bonding), with a Bi atom forming three σ bonds with its nearest neighbors,

and weak van der Waals bonding between two nearest-neighbor BLs (inter-BL bonding). The intra- and inter-BL sequence of bonds alternate along the $[111]$ stacking direction, which is exactly analogous to the alternating double and single bonds in polyacetylene shown schematically in Fig. 1(b-e).

Furthermore, as shown in Fig. 3(a), the intra- and inter-BL bonds can be interchanged, resulting in two degenerate dimerized ground states with opposite dimerization parameters $\delta \equiv \Delta/\Delta_0 = \pm 1$. Here, Δ is the displacement of the two Bi atoms in the primitive cell along $[111]$ [Fig. 3(a)] in units of the lattice vector $c = |\vec{a}_1 + \vec{a}_2 + \vec{a}_3|$ (\vec{a}_i , $i = 1-3$ are primitive lattice vectors), and Δ_0 is the equilibrium displacement. The positively dimerized state can be obtained from the negatively dimerized state via a translation by a half lattice vector, or vice versa. In sharp contrast to 2D and 3D topological orders, the Zak phase is not invariant under such a translation.

Electronic Structure– Fig. 3(b) shows the tight-binding (see Appendix A) band structure with ($\delta = \pm 1$, red lines) and without ($\delta = 0$, blue lines) dimerization. The direct band gaps at the TRIM points L and T close at $\delta = 0$ where the parity eigenvalues of the states near the Fermi level reverse sign by the dimerization sign reversal, indicating band inversions at these TRIM points.

Parity– The number of negative-parity eigenstates at the TRIM points is listed in Table I for the two different dimerization states, $\delta = \pm 1$. The change of parity states upon dimerization reversal is also related to the multiple choices of inversion center. For instance, if one takes $(0, 0, 0)$ (the diagonal corner of the primitive cell) to be the inversion center instead of $(1/2, 1/2, 1/2)$ (the center of the primitive cell), the parity of the state changes as if the dimerization is reversed. This is because a structure with reversed dimerization is equivalent to one that is translated by half the cell diagonal.

Topological phases protected by time-reversal or crystalline symmetries should be independent of the choice of inversion

TABLE I. Number of negative parity states n_{λ}^- of the six occupied bands at the TRIM points for two dimerizations $\delta = \pm 1$, classified under the eigenvalues of the symmetry operations $\sigma^{(1\bar{1}0)}$, $\hat{C}_3^{(111)}$, and $\hat{C}_2^{(1\bar{1}0)}$. The origin of the parity operation is $(1/2, 1/2, 1/2)$ and the two-fold \hat{C}_2 rotation axis, $[1\bar{1}0]$ is normal to the σ mirror plane, $(1\bar{1}0)$. Only those TRIM points which are invariant under these symmetry operations are listed.

δ	λ TRIM	n_{λ}^- total	$\sigma^{(1\bar{1}0)}$		$\hat{C}_3^{(111)}$			$\hat{C}_2^{(1\bar{1}0)}$	
			$-i$	$+i$	$-\pi/3$	π	$+\pi/3$	$-\pi/2 + \pi/2$	$+\pi/2$
+1	Γ	0	0	0	0	0	0	0	0
	T	2	1	1	1	0	1	1	1
	F	4	2	2	-	-	-	2	2
	L	2	1	1	-	-	-	1	1
-1	Γ	0	0	0	0	0	0	0	0
	T	4	2	2	1	2	1	2	2
	F	4	2	2	-	-	-	2	2
	L	4	2	2	-	-	-	2	2

center as well as the sign of dimerization. Even though there is a parity sign flip at the L and T points, we show below that the well-known topological phases of bulk Bi are indeed intact under dimerization reversal by calculating the various topological indices: (i) ν_0 for STI under time-reversal symmetry, (ii) $\{\nu^{(\pi)}, \nu^{(\pm\pi/3)}\}$ for higher order topological insulator (HOTI) under the three-fold rotational symmetry \hat{C}_3 , and (iii) $\{\nu^{(\pi/2)}, \nu^{(-\pi/2)}\}$ for crystalline topological insulator (CTI) under the two-fold rotational symmetry \hat{C}_2 .

First, the STI \mathbb{Z}_2 phase, protected by time-reversal symmetry, is expressed in terms of the parity eigenvalues of the occupied states at the TRIM points as,

$$\nu_0 = \frac{1}{2} \sum_{\lambda}^{\text{TRIM}} n_{\lambda}^{-} \bmod 2, \quad (3)$$

$$= \frac{1}{2} (n_{\Gamma}^{-} + n_{T}^{-} + 3n_{F}^{-} + 3n_{L}^{-}) \bmod 2, \quad (4)$$

where n_{λ}^{-} is the number of occupied states with negative parity at the TRIM point λ . For both dimerized phases, we find $\nu_0 = 0$ corresponding to the trivial phase that is consistent with previous reports.^{26,27}

Next, the HOTI phase of Bi is verified by grouping occupied states at TRIM points into \hat{C}_3 symmetry subspace according to the rotation eigenvalues of $\exp(i\pi)$ and $\exp(\pm i\pi/3)$.²⁶ The fact that each subspace is closed under time-reversal symmetry allows the \mathbb{Z}_2 classification for each subspace. Among the TRIM points, only Γ and T points are invariant under the \hat{C}_3 rotation. On the other hand, for the remaining ($F_{1,2,3}$ and $L_{1,2,3}$) TRIM which are not invariant under \hat{C}_3 , one can construct linear combination of these three states (which transform into each other under three-fold rotation; $F_1 \rightarrow F_2 \rightarrow F_3 \rightarrow F_1$ as well as L_i) to render them \hat{C}_3 eigenstates (see Ref.²⁶ for more details). The number of linearly combined states with negative parity for the two subspaces are $n_{\alpha,\pi}^{-} = n_{\alpha}^{-}$ and $n_{\alpha,\pm\pi/3}^{-} = 2n_{\alpha}^{-} = 0 \pmod{2}$, where $\alpha \in \{F, L\}$. Thus, the topological invariant for the two subspaces are given by

$$\nu^{(\pi)} = \frac{1}{2} (n_{\Gamma,\pi}^{-} + n_{T,\pi}^{-} + n_{F}^{-} + n_{L}^{-}) \bmod 2, \quad (5)$$

$$\nu^{(\pm\pi/3)} = \frac{1}{2} \left(n_{\Gamma,\pi/3}^{-} + n_{T,\pi/3}^{-} + n_{\Gamma,-\pi/3}^{-} + n_{T,-\pi/3}^{-} \right) \bmod 2. \quad (6)$$

The dimerization sign reversal changes $n_{T,\pi}^{-}$ and n_{L}^{-} by two, while $\nu^{(\pi)}$ and $\nu^{(\pm\pi/3)}$ do not change under modulo 2. Hence, we confirm that the HOTI phase, $\nu^{(\pi)} = \nu^{(\pm\pi/3)} = 1$ is intact under the dimerization reversal.

Finally it was predicted that bismuth is also a first-order CTI protected by a two-fold rotational symmetry \hat{C}_2 around the $[1\bar{1}0]$ axis or its symmetric copies $[01\bar{1}]$ and $[\bar{1}01]$.²⁷ Similarly, with the classification above, the parity states can be divided into the \hat{C}_2 subspace according to the symmetry eigenvalues of $\exp(i\pi/2)$ and $\exp(-i\pi/2)$. In contrast to the HOTI classification, the \hat{C}_2 subspaces are mapped to each other by time-reversal symmetry, indicating $\nu^{(\pi/2)} = \nu^{(-\pi/2)}$. The four TRIM points $\{\Gamma, T, F_1, L_1\}$ are invariant under \hat{C}_2 . The remaining states at the $F_{2,3}$ and $L_{2,3}$ points, which are not invariant under \hat{C}_2 , can be linearly combined so that they become \hat{C}_2 eigenstates. The number of negative parity eigenvalues $n_{F,L}^{-}$ contributes equally to $\nu^{(\pi/2)}$ and $\nu^{(-\pi/2)}$ with a weighting factor of one. Thus, the topological indices are

given by

$$\nu^{(\pi/2)} = \frac{1}{2} (n_{\Gamma,\pi/2}^{-} + n_{T,\pi/2}^{-} + n_{F,\pi/2}^{-} + n_{L,\pi/2}^{-} + n_{F}^{-} + n_{L}^{-}) \bmod 2, \quad (7)$$

$$\nu^{(-\pi/2)} = \frac{1}{2} (n_{\Gamma,-\pi/2}^{-} + n_{T,-\pi/2}^{-} + n_{F,-\pi/2}^{-} + n_{L,-\pi/2}^{-} + n_{F}^{-} + n_{L}^{-}) \bmod 2. \quad (8)$$

Each subspace is found to have a strong topology since $\nu^{(\pi/2)} = \nu^{(-\pi/2)} = 5 \pmod{2}$ and $7 \pmod{2}$ for positive ($\delta = +1$) and negative ($\delta = -1$) dimerizations, respectively. Therefore, the rotational-symmetry-protected CTI phase is well reproduced and is confirmed to be intact under the dimerization reversal.

It is important to note that in contrast to the topological phases that are invariant under dimerization sign reversal, the Zak phase depends on the sign of dimerization (i.e., choice of the unit cell). For example, the Γ and T points are projected at the $\tilde{\Gamma}$ point of the (111) surface BZ [Fig. 3(c)] where the Zak phase at $\tilde{\Gamma}$ is determined by the parity eigenvalues,

$$\frac{1}{\pi} \phi_Z(\tilde{\Gamma}) = \frac{1}{2} (n_{\Gamma}^{-} + n_{T}^{-}) \bmod 2. \quad (9)$$

Here, $\phi_Z(\tilde{\Gamma}) = \pi$ and 0 for positive ($\delta = +1$) and negative ($\delta = -1$) dimerization, respectively. Furthermore, the F and L points are projected on the other surface TRIM point \tilde{M} , and the Zak phase at \tilde{M} ,

$$\frac{1}{\pi} \phi_Z(\tilde{M}) = \frac{1}{2} (n_{F}^{-} + n_{L}^{-}) \bmod 2, \quad (10)$$

is calculated to be identical to $\phi_Z(\tilde{\Gamma})$ for each dimerized state. Note that systems with a strong topological order exhibit different Zak phases at the two surface TRIM points, $\exp[i\phi_Z(\tilde{\Gamma}) + i\phi_Z(\tilde{M})] = -1$, or equivalently $\nu_0 = 1$ from Eq. (4).^{23,24} The right panels in Fig. 3(a) show the (111) surface terminations of the two dimerized states where the surface with low cleavage energy corresponds to the positive dimerization with π Zak phase. Surprisingly, the non-trivial phase emerges on the surface that cuts the weak bonds ($\delta = +1$) rather than the strong bonds ($\delta = -1$). This is counter-intuitive, especially when compared to the original 1D SSH model.

To corroborate the parity analysis, the hybrid Wannier charge centers (WCCs) are computed for the two dimerized states in the hexagonal structure having six Bi atoms (18 valence electrons) as shown in Fig. 4. Because of the inversion and time-reversal symmetries, the WCCs are mapped to symmetric copies as $r_i(\mathbf{k}) \rightarrow -r_i(\mathbf{k})$ and $r_i(\mathbf{k}) \rightarrow r_i(-\mathbf{k})$, respectively. For $\delta = +1$, there are two WCCs crossing the cell boundary $z/c = \pm 0.5$ at $\tilde{\Gamma}$ (\tilde{M}) which is equal to the negative parity difference, $|n_{\Gamma}^{-} - n_{T}^{-}| = 2$ ($|n_{F}^{-} - n_{L}^{-}| = 2$). Similarly, for $\delta = -1$, four (zero) WCCs cross the cell boundary at $\tilde{\Gamma}$ (\tilde{M}), which also agrees well with the difference of negative parity states. The factor 2 from the spin degeneracy can be decomposed by grouping the WCCs based on the mirror eigenvalues $\pm i$ on the $\tilde{\Gamma}$ - \tilde{M} plane (see Fig.4). The WCCs with mirror eigenvalues $-i$ and $+i$ are denoted by blue and red lines, respectively. It is clearly seen that the number of boundary-crossing WCCs in each subspace is reduced by half. For example, a single blue line passes the boundary in

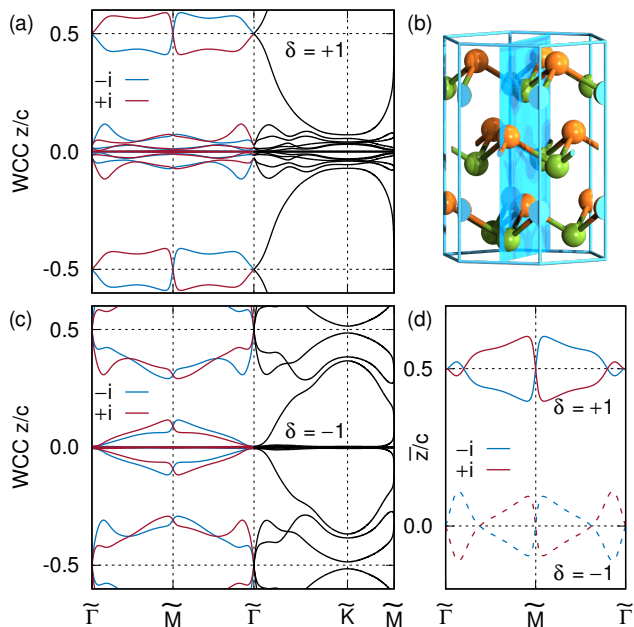


FIG. 4. Calculated Wannier charge centers (WCCs) of hexagonal Bi for (a) $\delta = +1$ and (c) $\delta = -1$. Blue (red) lines denote mirror irreps of $-i$ ($+i$) of the mirror plane shown in (b). (d) Integrated WCC where solid (dashed) lines correspond to $\delta = +1$ ($\delta = -1$).

Fig. 4(a). It agrees well with the mirror-symmetry-classified parity states in Table I where the negative parity states are divided in half ($n_{\lambda, \pm i}^- = (1/2)n_{\lambda}^-$) as well as their difference. Note that the number of negative parity states only provides an upper limit on the number of WCCs crossing the boundary, with the exact number of crossings being determined by the symmetry protection.²⁸ The net Wannier center $\bar{r} = \sum_i r_i$ is shown in Fig. 4(d), where the half polarization of the π Zak phase ($\delta = +1$) is clearly seen at the two TRIM, consistent with the parity results.

III. ANTIPHASE DOMAIN WALLS IN BI

The corresponding boundary states of the π Zak phase can be realized on the (111) surface by appropriate choice of the surface termination that is usually hard to control. Fortunately, Bi is found to exhibit the π Zak phase on the low-cleavage-energy surface. In general, however, the surface with π Zak phase is susceptible to reconstruction and contamination.¹² Thus, instead of the bare surface, we consider antiphase DWs across which the sign of dimerization is reversed, $\delta = \pm 1 \rightarrow \mp 1$, as shown in Fig. 5 and Fig. 7. The Bi (111) DWs, hosting the π Zak phase, is indeed the 3D analogue of the 1D SSH model. The DW is tolerant to chemical contamination and can easily be found in a system exhibiting charge density wave.

In order to study the DW state without the interference from the neighbor DW, we use the interface Green's function method^{29,30} where the central DW structure is sandwiched between two semi-infinite pristine Bi with opposite dimerizations, as is shown in Fig. 5(b,c) for the (111) DW and

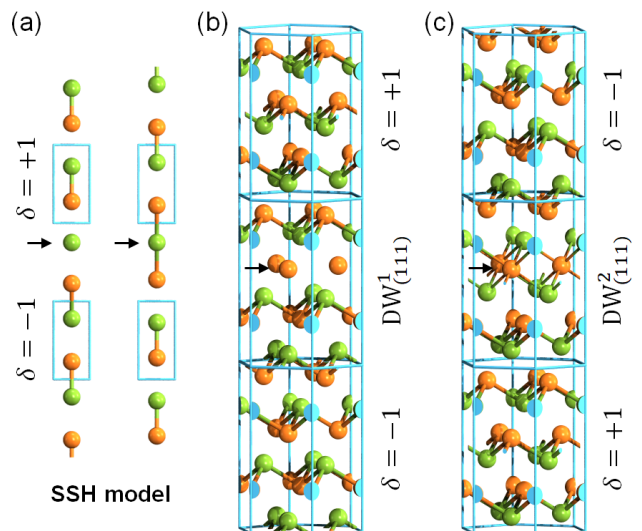


FIG. 5. (a) Schematic illustration of Su-Schrieffer-Heeger (SSH) model with two types of domain-wall (DW) interfaces. Blue rectangles denotes unit cells and the orange and green spheres indicate two sublattice sites. (b,c) Two types of Bi (111) DWs: (b) $DW_{(111)}^1$ and (c) $DW_{(111)}^2$, as the 3D analogues of the two DWs of the SSH model shown in (a). Hexagonal blocks with $\delta = \pm 1$ are the conventional cells with either of the dimerizations. The central hexagonal block denotes the interface where the sign of dimerization flips. Inversion symmetry is preserved in both DWs; the ion at the inversion center is marked with arrows.

Fig. 7(c,d) for the $(11\bar{2})$ DW. The construction of the Hamiltonian matrices is described in Appendix B. Throughout the remaining manuscript, the tilde (\sim) and bar ($-$) symbols over the k -point labels denote TRIM points on the (111) and $(11\bar{2})$ DW BZ, respectively.

A. Non-trivial (111) Domain Wall

DW localized states – We have considered two types of (111) DWs shown in Fig. 5(b,c). In type-I DW ($DW_{(111)}^1$) the semi-infinite regions below (above) the DW has $\delta = -1$ ($\delta = +1$) dimerization. The central DW region has an inversion center, denoted by the horizontal black arrow, located on an atomic layer which is weakly bonded with its neighboring atomic layers along the stacking direction. In type-II DW ($DW_{(111)}^2$), the sign of dimerization is opposite and the central layer has strong bondings in both directions. The $DW_{(111)}^1$ and $DW_{(111)}^2$ correspond to the two types of DWs of the SSH model shown in Fig. 5(a),

The calculated DW spectral function is shown in Fig. 6(a,b) where the DW localized states (yellow lines) emerge inside the DW-projected bulk states (blue shade). Since inversion symmetry is preserved at the DW, all bands including the DW-localized yellow bands are doubly degenerate. Note that, regarding the interface band degeneracy, the DW localized states resemble Fig. 2(d) instead of Fig. 2(e) even with strong SOC. This is due to the inversion symmetry at the DW in a sharp contrast to the bare surface where the inversion sym-

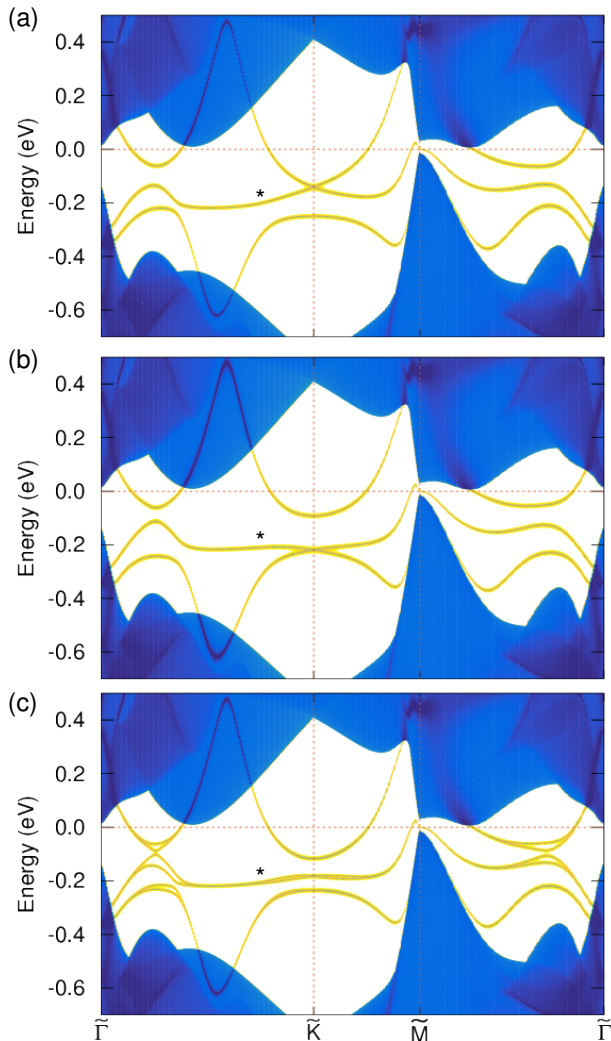


FIG. 6. (111) DW band structure calculated using the interface Green's function method for (a) $DW^1_{(111)}$, (b) $DW^2_{(111)}$, and (c) $DW^3_{(111)}$. DW-localized states (yellow lines) emerge inside DW-projected bulk states (blue shade). The DW localized band labeled with an asterisk is half-filled.

metry is always broken. The π Zak phase at $\tilde{\Gamma}$ and \tilde{M} points induces an odd number of bands inside the bandgap that guarantees at least one band to be pinned at the Fermi level as long as the chiral symmetry persists. We find three DW localized states which are buried in the bulk bands at $\tilde{\Gamma}$. At \tilde{M} , however, the second band in the middle among them appears inside the bandgap indicating adequate chiral symmetry at the \tilde{M} point compared to $\tilde{\Gamma}$.³¹ As discussed in Sec. I, the π Zak phase corresponds to half polarization resulting in $e/2$ modulo e surface charge per surface unit cell and half-filled in-gap state¹² (i.e., one electron per Kramers' pair³²). Integration of the spectral function at \tilde{M} indeed confirms the half-filling of the in-gap state in both types of DWs. The DW localized band, marked with asterisk in Fig. 6, which emerges from the non-trivial state at \tilde{M} is half-filled and hence metallic.

The number of DW-localized states can also be interpreted as the number of bonds truncated at the DW. On the (111) surface, a single Bi ion per unit cell is exposed with three bonds, consistent with the number of in-gap states. The number of bonds truncated at the DW is then determined by considering the Wannier function center, which is related to the Zak phase (see Eqs. 1 and 2). It is noteworthy that, for general systems with complicated terminations and reduced symmetries, a Green's function approach can rigorously predict the number of surface or interface in-gap states³³ without suffering from the ion-truncating termination¹¹ or lack of inversion symmetry. The metallic origin of the $DW^1_{(111)}$ can be simply understood from its construction involving the intercalation of a monolayer in pristine bulk Bi, which in turn introduces three doubly degenerate bands near the Fermi level, where the second band is half filled since the number of available electrons is three.

The emergence of 2D Dirac cones at \tilde{K} points in both DWs is unexpected and the crossing point is found to be lifted upon breaking the DW inversion symmetry. One way to break the inversion symmetry is to vertically translate the monolayer of $DW^1_{(111)}$. The translation eventually leads to a structure, equivalent to the $DW^2_{(111)}$, having a Bi tri-layer that recovers the inversion symmetry. Therefore, although the two DW structures [Fig. 5(b,c)] represent the 3D analogue of the SSH model, there is a general (111) DW structure without the DW inversion symmetry that will be referred to as type-III DW, $DW^3_{(111)}$ (see Appendix B for the DW Hamiltonian). Figure 6(c) shows the calculated band structure of $DW^3_{(111)}$ where the breakdown of inversion symmetry lifts the two-fold degeneracy of DW localized bands at generic k points except at the surface TRIM. One significant difference of $DW^3_{(111)}$, compared to the type-I and type-II DWs, is the splitting of the Dirac crossing at \tilde{K} , which in turn forms three separate bands, indicating that the Dirac cone is related to the DW inversion symmetry rather than the π Zak phase.

B. Trivial $(11\bar{2})$ Domain Wall

DW structure – In this section we consider two types of $(11\bar{2})$ DWs as shown in Fig. 7(c,d) where the dimerization [111] direction lies on the DW plane. Thus, the $(11\bar{2})$ DWs can not be directly compared with the SSH model, in contrast to the (111) DW where its dimerization direction is normal to the DW plane that is a natural extension of the 1D SSH model (Fig. 1). Nevertheless, this raises the question of the emergence of $(11\bar{2})$ DW localized states and their topological nature. In both DW types, the central DW region is sandwiched between two semi-infinite pristine regions with opposite dimerization, involving a rigid shift of the right semi-infinite region relative to the left along the $[111]$ direction by $(c/2)\hat{z}$, or vice versa. Detailed symmetries of the two DWs and consequent degeneracies of the band structure are further discussed in Appendix C.

DW Parity – Figure 3(c) shows the bulk and $(11\bar{2})$ interface BZs, where the bulk TRIM points are projected on the following interface TRIM points,

$$\Gamma, F \rightarrow \bar{\Gamma}; \quad F, F \rightarrow \bar{Y}; \quad T, L \rightarrow \bar{Z}; \quad L, L \rightarrow \bar{T}. \quad (11)$$

The parity flip induced by the dimerization reversal occurs at both the T and L points which are projected on the \bar{Z} and \bar{T} points of the $(11\bar{2})$ interface BZ. Since the difference in the

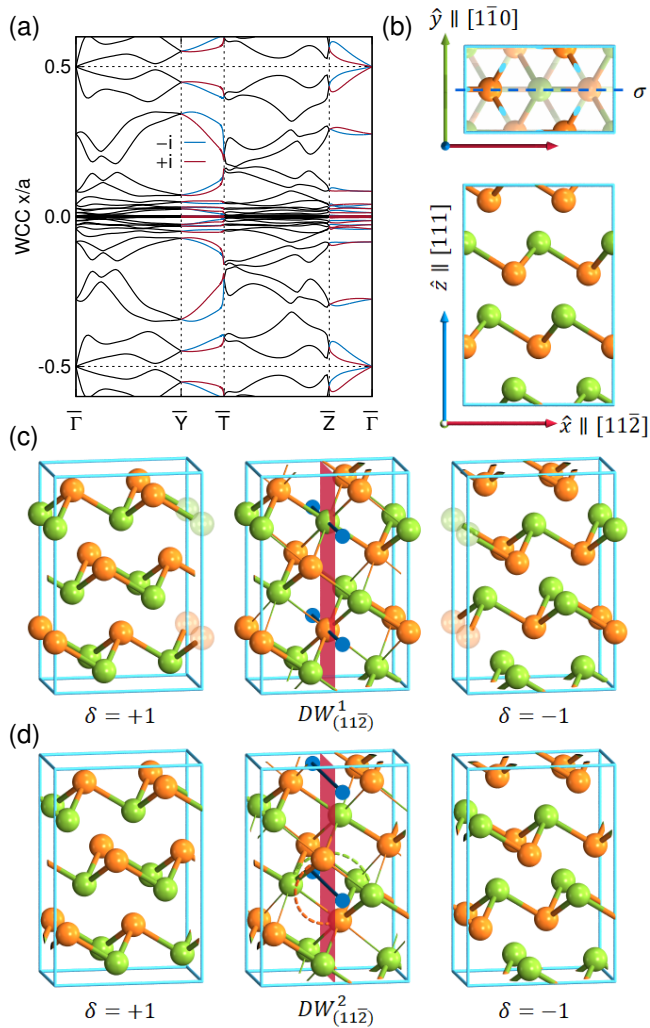


FIG. 7. Bi $(11\bar{2})$ domain wall (DW) structure: (a) Calculated Wannier charge center (WCC) of the slab structure ($\delta = +1$) shown in (c). Blue and red lines denote mirror irreps of $-i$ and $+i$, respectively. (b) Top-down and side views of the orthogonal unit cell, where σ denotes the mirror plane. Two types of $(11\bar{2})$ DWs: (c) $DW^1_{(11\bar{2})}$ and (d) $DW^2_{(11\bar{2})}$, where the red plane denotes the DW and the blue axes with disks at the end denote the rotation or screw axes. The central DW region is sandwiched between two semi-infinite pristine regions with opposite dimerization. Type-I DW, $DW^1_{(11\bar{2})}$, passes through the ions and has inversion, mirror, and two-fold rotation symmetries. Type-II DW, $DW^2_{(11\bar{2})}$ has the same symmetries but with the two-fold rotation replaced with the screw operation, denoted by the dashed curve.

number of parity flips (Table I) between the two dimerized domains is zero at $\bar{\Gamma}$ and \bar{Y} and four at \bar{Z} and \bar{T} , the DW-projected Zak phases of both domains are the same, indicating the trivial topology of the DW states for both types of $(11\bar{2})$ DWs, unless certain crystal symmetry separates each band inversion. Since the mirror plane σ in Fig. 7(b) is common in both domains and the DWs one can group the parity states according to the mirror eigenvalues. Fig. 7(a) displays the hybrid WCCs labeled by the mirror-symmetry eigenvalues on

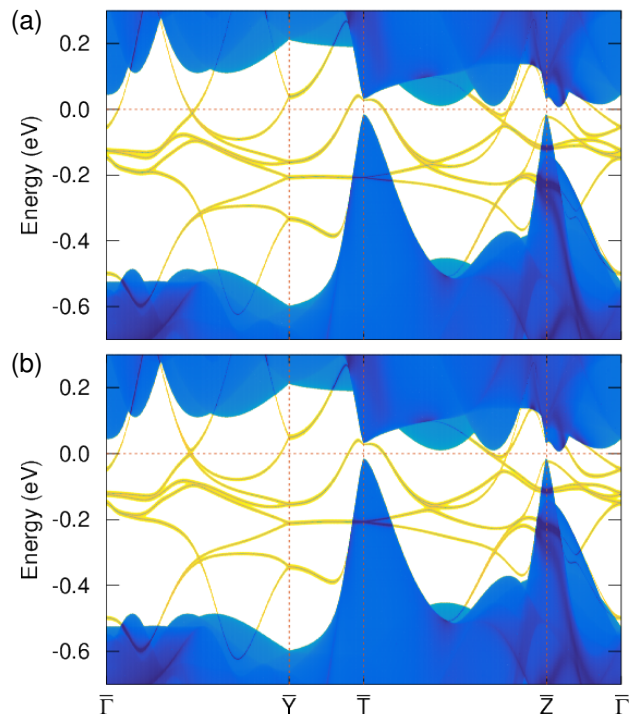


FIG. 8. $(11\bar{2})$ DW band structures calculated using the interface Green's function method for (a) $DW^1_{(11\bar{2})}$ and (b) $DW^2_{(11\bar{2})}$, where the spin-degenerate DW-localized bands (yellow lines) emerge in the DW-projected bulk bands (blue shade).

$\bar{\Gamma} - \bar{Z}$ and $\bar{Y} - \bar{T}$, which shows no evidence for non-trivial DW state.

DW localized states and symmetry – The band structures of the $DW^1_{(11\bar{2})}$ and $DW^2_{(11\bar{2})}$ are shown in Fig. 8, where eight of spin-degenerate DW-localized bands (yellow lines) appear inside the DW-projected bulk states (blue shade). The number of DW localized bands is related to the number of truncated bonds on the $(11\bar{2})$ plane which are eight in both DWs (see red planes in Fig. 7(c,d)). The fact that the number of in-gap states is even is consistent with the trivial Zak phase determined from the product of parity eigenvalues. Because of the complicated band dispersion and crossings of the DW localized states, we focus only on the high symmetry line $\bar{Y} - \bar{T}$ on which the DW localized states are approximately four-fold degenerate. We find no specific crystal symmetry protecting such degeneracy. Nevertheless, an effective symmetry can be defined which can give rise to such degeneracy in the thick DW limit (Appendix C).

C. Arbitrary DW orientation

So far, we have considered Bi antiphase DW as a 3D analog of the SSH model with DW orientation either perpendicular or parallel to the dimerization direction. For the (111) DW, the projected parity flips across the DW inducing the π Zak phase while the Zak phase is 0 for the $(11\bar{2})$ DW. In order to

TABLE II. List of projection of the eight bulk TRIM points $\lambda_{\{n_i\}}$, each labeled by the set of integers (n_1, n_2, n_3) , [Eq. (13)] on a general surface or interface plane with Miller indices (m_1, m_2, m_3) , labeled as odd (o) or even (e) [see Eq. (15)]. Also we list the four pairs of TRIM points which overlap on the projected 2D BZ.

	TRIM	Miller indices	Pair of TRIM
$\lambda_{\{n_i\}}$	(n_1, n_2, n_3)	(m_1, m_2, m_3)	
k_1	(0,0,0)	(e,e,e)	-
k_2	(1,0,0)	(o,e,e)	$\{k_1 k_2, k_3 k_7, k_4 k_6, k_5 k_8\}$
k_3	(0,1,0)	(e,o,e)	$\{k_1 k_3, k_2 k_7, k_4 k_5, k_6 k_8\}$
k_4	(0,0,1)	(e,e,o)	$\{k_1 k_4, k_2 k_6, k_3 k_5, k_7 k_8\}$
k_5	(0,1,1)	(e,o,o)	$\{k_1 k_5, k_6 k_7, k_2 k_8, k_3 k_4\}$
k_6	(1,0,1)	(o,e,o)	$\{k_1 k_6, k_5 k_7, k_2 k_4, k_3 k_8\}$
k_7	(1,1,0)	(o,o,e)	$\{k_1 k_7, k_5 k_6, k_2 k_3, k_4 k_8\}$
k_8	(1,1,1)	(o,o,o)	$\{k_1 k_8, k_2 k_5, k_3 k_6, k_4 k_7\}$

predict the general behavior of the Zak phase for different DW orientations, we consider the possible ways of projecting the bulk TRIM points on various DW planes. For a surface or DW plane with Miller indices (m_1, m_2, m_3) , the surface/interface normal vector is given by,

$$\mathbf{G}_{\{m_i\}} = m_1 \mathbf{b}_1 + m_2 \mathbf{b}_2 + m_3 \mathbf{b}_3, \quad (12)$$

where the \mathbf{b}_i 's are reciprocal lattice vectors and the $\{m_i\} \in \mathbb{Z}$ have no common factor. A pair of bulk TRIM points $\{\lambda_{\{n_i\}}, \lambda_{\{n_i^0\}}\}$ projected at the same point of the surface/interface BZ are always separated by $\mathbf{G}_{\{m_i\}}/2$, that is given by,

$$\lambda_{\{n_i\}} = \frac{1}{2}(n_1 \mathbf{b}_1 + n_2 \mathbf{b}_2 + n_3 \mathbf{b}_3), \quad (13)$$

$$\lambda_{\{n_i\}} - \lambda_{\{n_i^0\}} + \mathbf{G} = \frac{1}{2} \mathbf{G}_{\{m_i\}} \quad (14)$$

where $n_i = \{0, 1\}$ selects one TRIM point out of the eight and \mathbf{G} is an appropriate reciprocal lattice translation. The pair of TRIM points $\{\lambda_n, \lambda_{n^0}\}$ satisfy the following relation,

$$n_i = n_i^0 + m_i - 2|\mathbf{G}_i| = (n_i^0 + m_i) \bmod 2. \quad (15)$$

This demonstrates that the n_i and n_i^0 are identical if the Miller index m_i is even, otherwise they differ by one if m_i is odd. Using this relation, one can enumerate all possible pairs of TRIM points which overlap on the projected 2D BZ of an arbitrary surface or DW, which are listed in Table II. The (111) and (11 $\bar{2}$) DWs correspond to (o,o,o) and (o,o,e) indices, respectively. The parity sign flip of Bi induced by dimerization reversal occurs at k_2, k_3, k_4 , and k_8 points in this notation. The antiphase DWs with Miller indices (e,e,o), (e,o,e), and (o,e,e) are expected to have parity sign flip across the DW giving rise to DW-localized states similar to the (111) DW or the SSH model. The remaining (e,o,o) and (o,e,o) DWs are expected to be trivial similar to the (11 $\bar{2}$) DW. It is important to emphasize that since Table II is valid for arbitrary reciprocal lattice vectors, \mathbf{b}_i ($i = 1 - 3$), it can be applied to a general centrosymmetric system. The only information required to predict a non-trivial DW orientation is to determine which TRIM point flips its parity product across the DW. It is even easier for bare surfaces, where the parity eigenvalues of the ground state are enough to predict a non-trivial surface orientation.

D. Experimental Realization of Dimerization Reversal via Optical Pumping

There are two plausible experimental approaches to realize Bi antiphase DWs. The first approach is to search for dislocation defects in a Bi single crystal. For example, the (11 $\bar{2}$) DW would appear on the (111) surface as a half step edge (step height of Bi monolayer, $c/6$) in scanning tunneling microscopy measurements. The second approach is to induce local dimerization reversal in pristine Bi using intense femtosecond laser-pump excitations, which have shown the reduction of the equilibrium displacement (Δ_0) of Bi, referred to as ‘‘ultrafast bond softening’’.²⁵ More specifically, the laser-pump promotes valence electron into the conduction band and softens the Bi bond that agrees well with complementary density functional theory calculations.²⁵ The calculations also predict a transient structural transition to undimerized state ($\Delta_0 \rightarrow 0$) upon excitation of $\sim 2.5\%$ of valence electrons. The energy barrier between the two dimerized ground states was found to decrease with increasing charge excitations, thus supporting the plausibility of dimerization reversal by excitations. Indeed, experiments confirmed that excitations higher than 2% lead to an irreversible ‘‘damage’’ to the samples suggesting that a permanent dimerization reversal may be achieved via the laser-pump excitations.²⁵

IV. CONCLUSION

We propose that the α -phase of bulk Bi is a 3D manifestation of the SSH model. We demonstrate that while the HOTI and CTI phases of bulk Bi remain invariant under dimerization sign reversal, the Zak phase undergoes a transition from π to 0. The (111) antiphase DW is found to host metallic DW bands, which are topologically protected due to the difference in polarization between the two oppositely dimerized domains (i.e., π Zak phase), which is the 3D analogue of the SSH model. Although the (11 $\bar{2}$) DW has no such polarization difference, the DW localized states exhibit interesting behavior related to an effective symmetry that reveals itself in thicker DWs.

To the best of our knowledge, this result is the first demonstration of the non-trivial Zak phase in 3D antiphase DWs. Unlike the bare surface being vulnerable to doping, contamination, or reconstruction, antiphase DWs offer a relatively stable platform for the manifestation of a non-trivial Zak phase. Furthermore, the common presence of DWs in charge-density-wave states offers a novel venue for investigating the potential of the non-trivial Zak phase.

V. METHODOLOGY

The tight-binding parameters are extracted from the Wannier Hamiltonian obtained by using VASP-Wannier90 interface.³⁴⁻³⁶ The pseudopotentials are of the projector-augmented-wave type as implemented in VASP,^{37,38} with valence configurations $6s^2 6p^3$ for Bi. The exchange-correlation functional is described by the Perdew-Burke-Ernzerhof generalized gradient approximation (PBE).³⁹ The plane-wave cutoff energy is set to 300 eV and the Brillouin zone sampling grid is $12 \times 12 \times 12$. The structure is relaxed with a constraint of

being FCC for an insulating band gap. The twelve strongest hopping terms are then used in the calculation together with atomic spin-orbit coupling for the p orbitals. The spectral density of DW-localized states is calculated using the interface Green's function method^{29,30} where two semi-infinite surface Green's functions are first calculated for the two dimerized phases and then combined with the central DW Hamiltonian.

ACKNOWLEDGMENTS

This work at CSUN is supported by the NSF-Partnership in Research and Education in Materials (PREM) Grant No. DMR-1205734. D.V. was supported by NSF Grant DMR-1954856.

Appendix A: Tight-binding parameters

Although Bi has finite direct band gap in the whole BZ, its indirect gap between T and L points is negative causing metallic band structure and difficulties in the analysis of topological properties. For instance, the projected bulk states (blue shade in Fig. 8) at the \bar{Z} point on the $(11\bar{2})$ BZ, should be gapless due to the negative indirect gap. In order to suppress the complexity, we have constructed the tight-binding parameters in the fcc instead of the rhombohedral cell, which in turn opens up a gap, shown in Fig. 3(b), without affecting the topological properties such as parities at the TRIM points.

Figure 9 shows the selected twelve hopping terms in a dimerized cubic lattice and the amplitudes are listed in the inset table together with that of the atomic spin-orbit coupling.

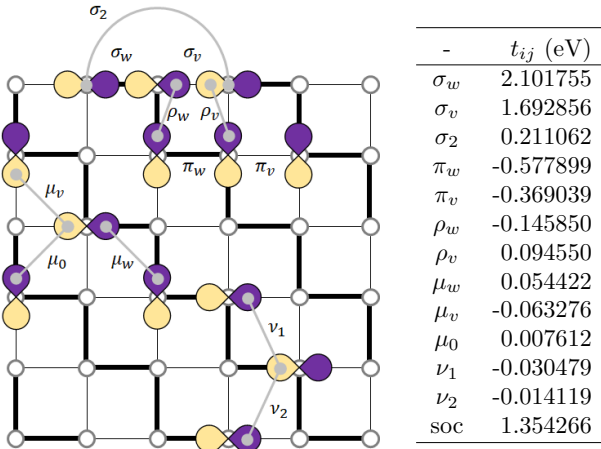


FIG. 9. Selected tight-binding parameters for Bi. The background square lattice illustrates the Bi plane normal to one of the Cartesian coordinate vectors. Thick (thin) black line denotes strong (weak) bonding after the atomic displacement (i.e. dimerization). The hopping terms with subscripts, w and v , are lifted by the dimerization and they are swapped by the dimerization reversal. Terms with numerical subscripts are not affected by the dimerization reversal.

The $\sigma_{w,v}$, $\pi_{w,v}$, and $\rho_{w,v}$ are the nearest-neighbor hoppings distinguished by the relative direction of the p orbitals; the σ_2 is the third nearest-neighbor σ -bond like hopping term; the $\rho_{w,v}$ terms vanish without dimerization because of the basis symmetry; the $\mu_{w,v,0}$ and $\nu_{1,2}$ terms are the second nearest-neighbor hoppings, and the $\nu_{1,2}$ terms do not change under dimerization reversal unless the direction of dimerization changes.

Appendix B: Hamiltonian of the DW

The hopping terms with subscripts w and v modulate in the vicinity of the DW. The amplitude of the hopping terms is determined via linear interpolation of the two hopping terms by considering the distances of two basis from the DW plane. Namely,

$$t'_{ij}{}^w = (1 - r_{ij})t_{ij}{}^w + r_{ij}t_{ij}{}^v, \quad (\text{B1})$$

$$t'_{ij}{}^v = (1 - r_{ij})t_{ij}{}^v + r_{ij}t_{ij}{}^w, \quad (\text{B2})$$

$$r_{ij} = (w_i + w_j + 4)/8, \quad (\text{B3})$$

where t_{ij} is the original hopping terms of Bi (Fig. 9) and r_{ij} is the mixing ratio depending on the weight factor w_i representing the sign of dimerization as illustrated in Fig. 10 and 11. The $DW_{(111)}^1$ and $DW_{(111)}^2$ have 6 atomic layers along the stacking direction with one ion per layer. The $DW_{(11\bar{2})}^1$ has 14 ions and 7 vertical planes (w_1, \dots, w_7) in the cell while $DW_{(11\bar{2})}^2$ has 12 ions and 6 vertical planes. In this interpolation scheme, the weighting factors for the thinnest $(11\bar{2})$ DW are also listed with a subscript “thin” in the inset of Fig. 11. The results for thin DW case shown in Fig.12(b,d) are calculated using Hamiltonians generated with these weighting factors.

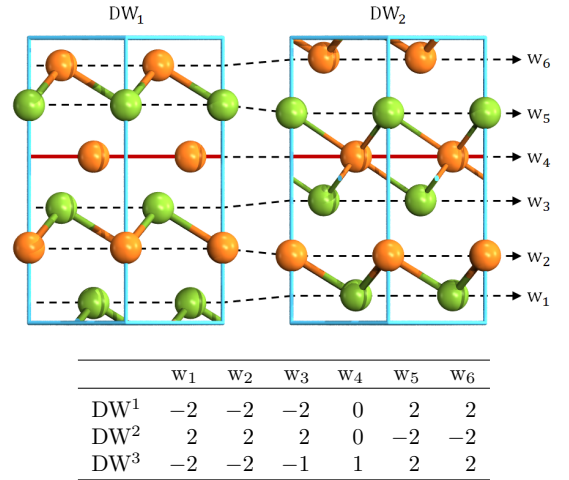


FIG. 10. Modulation of hopping parameters across the (111) DW. Two types of DWs are illustrated together with horizontal planes, separated from the DW denoted as red solid line. Weight factors used for the linear interpolation are presented in the inset table together with the type-III DW.

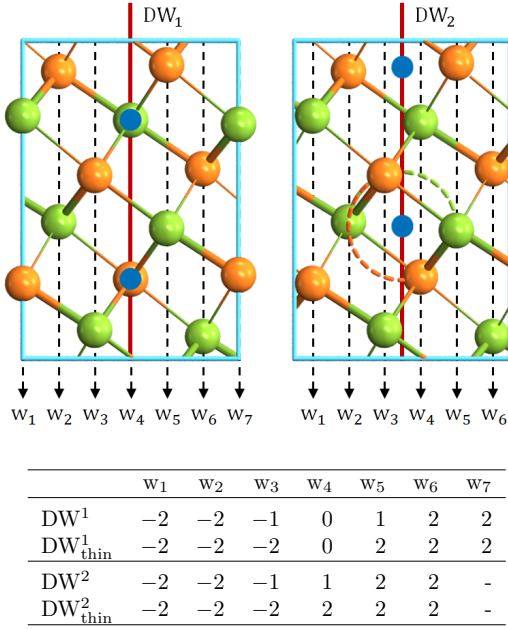


FIG. 11. Modulation of hopping parameters across the $(11\bar{2})$ DW. Two types of DWs are illustrated together with vertical planes, separated from the DW denoted as red solid line. Weight factors used for the linear interpolation are presented in the inset table.

Appendix C: Symmetry of $(11\bar{2})$ DW

In type-I DW, $DW^1_{(11\bar{2})}$, [Fig. 7(c)] where the Bi atoms lie on the DW plane, has inversion, mirror, and two-fold rotation symmetries. The two-fold rotation, \hat{C}_2 around the $[1\bar{1}0]$ direction is denoted by the horizontal blue axis. On the other hand, type-II DW, $DW^2_{(11\bar{2})}$, [Fig. 7(d)] intersects the bonds between atoms across the DW and has similar symmetries as $DW^1_{(11\bar{2})}$ except that the \hat{C}_2 rotation is replaced by a screw \hat{S}_2 symmetry involving a two-fold rotation around the $[1\bar{1}0]$ direction followed by a half a translation along the same axis. Namely,

$$\hat{C}_2 : (x, y, z) \rightarrow (-x, y, -z) \otimes i\sigma_y, \quad (C1)$$

$$\hat{S}_2 : (x, y, z) \rightarrow (-x, y + 1/2, -z) \otimes i\sigma_y. \quad (C2)$$

Because of the DW inversion symmetry, all bands are two-fold degenerate in the whole interface BZ. The high symmetry lines along k_y ($\bar{\Gamma} - \bar{Y}$ and $\bar{Z} - \bar{T}$) are invariant under the \hat{C}_2 operation for the $DW^1_{(11\bar{2})}$ and the \hat{S}_2 operation for the $DW^2_{(11\bar{2})}$. In addition, the nonsymmorphic \hat{S}_2 symmetry for $DW^2_{(11\bar{2})}$ guarantees a four-fold degeneracy at \bar{Y} and \bar{T} where $k_y = \pm\pi$.⁴⁰

In Fig. 12(a,c) we display the zoom-in band structure of Fig. 8(a,b) on the high symmetry line $\bar{Y} - \bar{T}$ for both types of DWs along with the corresponding k -resolved spectral function (blue lines) at \bar{Y} . The calculations of the spectral function for $DW^2_{(11\bar{2})}$ corroborate the emergence of single peaks at

\bar{Y} which are indeed four-fold degenerate. On the other hand, such a four-fold degeneracy is not protected by \hat{C}_2 symmetry for $DW^1_{(11\bar{2})}$, which, however, exhibits similar band folding at \bar{Y} point, where the peaks in Fig. 12(a) have negli-

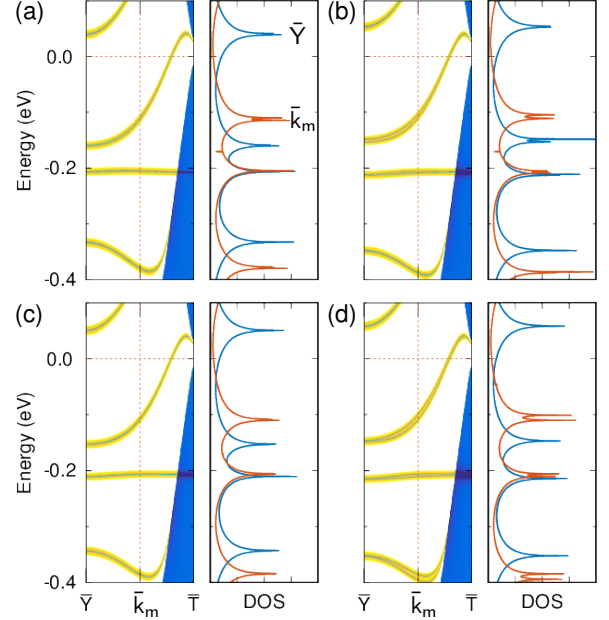


FIG. 12. Zoom-in band structure (left panel) and k -resolved spectral function (right panel) for (a,b) $DW^1_{(11\bar{2})}$ and (c,d) $DW^2_{(11\bar{2})}$. The spectral functions at \bar{Y} (blue line) and \bar{k}_m (red line) points are plotted in log scale. (b) and (d) are similar plots for thinner DW width than (a) and (c), respectively, showing the splitting of the peaks.

ble splitting. Furthermore, the high symmetry line $\bar{Y} - \bar{T}$ appears to be four fold degenerate in both types of DWs, which cannot not be explained by the crystal symmetries. This apparent four-fold degeneracy of the high symmetry line is found to be lifted as the DW thickness is reduced, as is clearly shown by the splitting of the peaks (denoted by red) in Fig. 12(b,d). This implies an effective symmetry which appears to be present only for thicker DWs.

It is worth to emphasize that the two types of DWs are distinguished only by the position of DW plane and the Hamiltonian difference between the two DWs becomes subtle with increasing DW thickness. Both Hamiltonians eventually acquire \hat{C}_2 and \hat{S}_2 symmetries in the thick DW limit. The two symmetries are combined to an effective symmetry of the DW which can be expressed as

$$\hat{C}_2\hat{S}_2 : (x, y, z) \rightarrow (x, y + 1/2, z) \otimes -1, \quad (C3)$$

consisting of a half translation operation that allows the BZ-unfolding, $k_y: [-\pi; +\pi] \rightarrow [-2\pi; +2\pi]$ and causes band degeneracy on the $k_y = \pm\pi$ line. This emergent half translation symmetry naturally explains the apparent four-fold degeneracy (i) of the high symmetry line $\bar{Y} - \bar{T}$ in both types of DWs, and (ii) at \bar{Y} in $DW^1_{(11\bar{2})}$.

- ¹ Alan J. Heeger, “Nobel lecture: Semiconducting and metallic polymers: The fourth generation of polymeric materials,” *Rev. Mod. Phys.* **73**, 681–700 (2001).
- ² W. P. Su, J. R. Schrieffer, and A. J. Heeger, “Solitons in polyacetylene,” *Phys. Rev. Lett.* **42**, 1698–1701 (1979).
- ³ W. P. Su, J. R. Schrieffer, and A. J. Heeger, “Soliton excitations in polyacetylene,” *Phys. Rev. B* **22**, 2099–2111 (1980).
- ⁴ J. Zak, “Berry’s phase for energy bands in solids,” *Phys. Rev. Lett.* **62**, 2747–2750 (1989).
- ⁵ A Yu Kitaev, “Unpaired majorana fermions in quantum wires,” *Physics-uspekhi* **44**, 131 (2001).
- ⁶ Xiang-Long Yu, Liang Jiang, Ya-Min Quan, Tong Wu, Yuanzhen Chen, Liang-Jian Zou, and Jiansheng Wu, “Topological phase transitions, majorana modes, and quantum simulation of the su–schrieffer–heeger model with nearest-neighbor interactions,” *Phys. Rev. B* **101**, 045422 (2020).
- ⁷ P. Delplace, D. Ullmo, and G. Montambaux, “Zak phase and the existence of edge states in graphene,” *Phys. Rev. B* **84**, 195452 (2011).
- ⁸ Feng Liu and Katsunori Wakabayashi, “Novel topological phase with a zero berry curvature,” *Phys. Rev. Lett.* **118**, 076803 (2017).
- ⁹ Daichi Obana, Feng Liu, and Katsunori Wakabayashi, “Topological edge states in the su–schrieffer–heeger model,” *Phys. Rev. B* **100**, 075437 (2019).
- ¹⁰ Linghua Zhu, Emil Prodan, and Keun Hyuk Ahn, “Flat energy bands within antiphase and twin boundaries and at open edges in topological materials,” *Phys. Rev. B* **99**, 041117(R) (2019).
- ¹¹ Motoaki Hirayama, Satoru Matsuishi, Hideo Hosono, and Shuichi Murakami, “Electrides as a new platform of topological materials,” *Phys. Rev. X* **8**, 031067 (2018).
- ¹² Yusuke Aihara, Motoaki Hirayama, and Shuichi Murakami, “Anomalous dielectric response in insulators with the π zak phase,” *Phys. Rev. Research* **2**, 033224 (2020).
- ¹³ Yunwei Zhang, Hui Wang, Yanchao Wang, Lijun Zhang, and Yanming Ma, “Computer-assisted inverse design of inorganic electrides,” *Phys. Rev. X* **7**, 011017 (2017).
- ¹⁴ Shinsei Ryu and Yasuhiro Hatsugai, “Topological origin of zero-energy edge states in particle-hole symmetric systems,” *Phys. Rev. Lett.* **89**, 077002 (2002).
- ¹⁵ A. A. Burkov, M. D. Hook, and Leon Balents, “Topological nodal semimetals,” *Phys. Rev. B* **84**, 235126 (2011).
- ¹⁶ Chen Fang, Hongming Weng, Xi Dai, and Zhong Fang, “Topological nodal line semimetals,” *Chinese Physics B* **25**, 117106 (2016).
- ¹⁷ David Vanderbilt and R. D. King-Smith, “Electric polarization as a bulk quantity and its relation to surface charge,” *Phys. Rev. B* **48**, 4442–4455 (1993).
- ¹⁸ Manuel Smeu, Hong Guo, Wei Ji, and Robert A. Wolkow, “Electronic properties of $\text{si}(111)\text{-}7 \times 7$ and related reconstructions: Density functional theory calculations,” *Phys. Rev. B* **85**, 195315 (2012).
- ¹⁹ M. V. Berry, “Quantal phase factors accompanying adiabatic changes,” *Proc. R. Soc. Lond. A* **392**, 45–57 (1984).
- ²⁰ R. D. King-Smith and David Vanderbilt, “Theory of polarization of crystalline solids,” *Phys. Rev. B* **47**, 1651–1654 (1993).
- ²¹ Raffaele Resta, “Macroscopic polarization in crystalline dielectrics: the geometric phase approach,” *Rev. Mod. Phys.* **66**, 899–915 (1994).
- ²² Jun-Won Rhim, Jan Behrends, and Jens H. Bardarson, “Bulk-boundary correspondence from the intercellular zak phase,” *Phys. Rev. B* **95**, 035421 (2017).
- ²³ Liang Fu, C. L. Kane, and E. J. Mele, “Topological insulators in three dimensions,” *Phys. Rev. Lett.* **98**, 106803 (2007).
- ²⁴ Liang Fu and C. L. Kane, “Topological insulators with inversion symmetry,” *Phys. Rev. B* **76**, 045302 (2007).
- ²⁵ D. M. Fritz, D. A. Reis, B. Adams, R. A. Akre, J. Arthur, C. Blome, P. H. Bucksbaum, A. L. Cavalieri, S. Engemann, S. Fahy, R. W. Falcone, P. H. Fuoss, K. J. Gaffney, M. J. George, J. Hajdu, M. P. Hertlein, P. B. Hillyard, M. Horn von Hoegen, M. Kammler, J. Kaspar, R. Kienberger, P. Krejčík, S. H. Lee, A. M. Lindenberg, B. McFarland, D. Meyer, T. Montagne, Éamonn D. Murray, A. J. Nelson, M. Nicoul, R. Pahl, J. Rudati, H. Schlarb, D. P. Siddons, K. Sokolowski-Tinten, Th. Tschentscher, D. von der Linde, and J. B. Hastings, “Ultrafast bond softening in bismuth: Mapping a solid’s interatomic potential with x-rays,” *Science* **315**, 633–636 (2007), <https://www.science.org/doi/pdf/10.1126/science.1135009>.
- ²⁶ Frank Schindler, Zhijun Wang, Maia G. Vergniory, Ashley M. Cook, Anil Murani, Shamashis Sengupta, Alik Yu. Kasumov, Richard Deblock, Sangjun Jeon, Ilya Drozdov, H el ene Bouchiat, Sophie Gu eron, Ali Yazdani, B. Andrei Bernevig, and Titus Neupert, “Higher-order topology in bismuth,” *Nature Physics* **14**, 918–924 (2018).
- ²⁷ Chuang-Han Hsu, Xiaoting Zhou, Tay-Rong Chang, Qiong Ma, Nuh Gedik, Arun Bansil, Su-Yang Xu, Hsin Lin, and Liang Fu, “Topology on a new facet of bismuth,” *Proceedings of the National Academy of Sciences* **116**, 13255–13259 (2019), <https://www.pnas.org/doi/pdf/10.1073/pnas.1900527116>.
- ²⁸ A. Alexandradinata, Xi Dai, and B. Andrei Bernevig, “Wilson-loop characterization of inversion-symmetric topological insulators,” *Phys. Rev. B* **89**, 155114 (2014).
- ²⁹ M P Lopez Sancho, J M Lopez Sancho, J M L Sancho, and J Rubio, “Highly convergent schemes for the calculation of bulk and surface green functions,” *Journal of Physics F: Metal Physics* **15**, 851–858 (1985).
- ³⁰ Taisuke Ozaki, Kengo Nishio, and Hiori Kino, “Efficient implementation of the nonequilibrium green function method for electronic transport calculations,” *Phys. Rev. B* **81**, 035116 (2010).
- ³¹ Our tight-binding parameters are tuned to open an insulating gap at, for example, $\bar{\Gamma}$, that is otherwise closed due to the overlap of electron and hole pockets (refers to Appendix A for details). The buried DW localized state, therefore, does not worsen the topological property of the DW.
- ³² Fan Zhang, C. L. Kane, and E. J. Mele, “Time-reversal-invariant topological superconductivity and majorana kramers pairs,” *Phys. Rev. Lett.* **111**, 056402 (2013).
- ³³ Jun-Won Rhim, Jens H. Bardarson, and Robert-Jan Slager, “Unified bulk-boundary correspondence for band insulators,” *Phys. Rev. B* **97**, 115143 (2018).
- ³⁴ G. Kresse and J. Furthm uller, “Efficient iterative schemes for ab initio total-energy calculations using a plane-wave basis set,” *Phys. Rev. B* **54**, 11169–11186 (1996).

- ³⁵ G. Kresse and J. Furthmüller, “Efficiency of ab-initio total energy calculations for metals and semiconductors using a plane-wave basis set,” *Computational Materials Science* **6**, 15 – 50 (1996).
- ³⁶ Arash A. Mostofi, Jonathan R. Yates, Giovanni Pizzi, Young-Su Lee, Ivo Souza, David Vanderbilt, and Nicola Marzari, “An updated version of wannier90: A tool for obtaining maximally-localised wannier functions,” *Comput. Phys. Commun.* **185**, 2309 – 2310 (2014).
- ³⁷ P. E. Blöchl, “Projector augmented-wave method,” *Phys. Rev. B* **50**, 17953–17979 (1994).
- ³⁸ G. Kresse and D. Joubert, “From ultrasoft pseudopotentials to the projector augmented-wave method,” *Phys. Rev. B* **59**, 1758–1775 (1999).
- ³⁹ John P. Perdew, Kieron Burke, and Matthias Ernzerhof, “Generalized gradient approximation made simple,” *Phys. Rev. Lett.* **77**, 3865–3868 (1996).
- ⁴⁰ Steve M. Young and Charles L. Kane, “Dirac semimetals in two dimensions,” *Phys. Rev. Lett.* **115**, 126803 (2015).